Large Deflection Dynamics and Control for Planar Continuum Robots

Ian A. Gravagne, *Member, IEEE*, Christopher D. Rahn, and Ian D. Walker, *Senior Member, IEEE*

Abstract—This paper focuses on a class of robot manipulators termed "continuum" robots—robots that exhibit behavior similar to tentacles, trunks, and snakes. In previous work, we studied details of the mechanical design, kinematics, path-planning and small-deflection dynamics for continuum robots such as the Clemson "Tentacle Manipulator." In this paper, we discuss the dynamics of a planar continuum backbone section, incorporating a large-deflection dynamic model. Based on these dynamics, we formulate a vibration-damping setpoint controller, and include experimental results to illustrate the efficacy of the proposed controller.

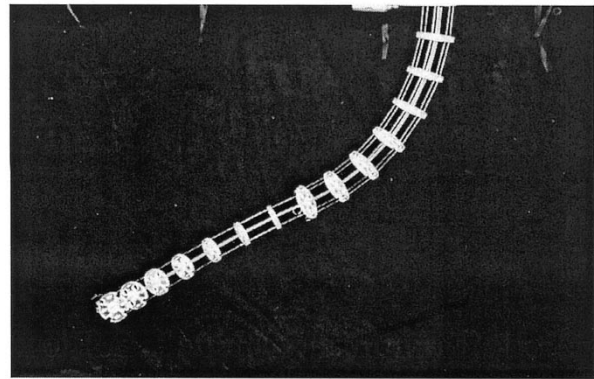*Index Terms*—Continuum manipulator, dynamics, flexible robot control, hyper-redundant robot.

Fig. 1. Clemson tentacle manipulator. The manipulator consists of two independent sections on a continuous backbone consisting of a thin elastic rod.

I. INTRODUCTION

NATURE motivates the study and design of hyper-redundant and continuum robots. Although nature often meets locomotive and manipulative needs with rigid-link designs, some creatures benefit greatly from continuum (or nearly continuum) arrangements. Examples include snake backbones, elephants' trunks, squid and octopus tentacles, and a host of smaller animals such as worms, various larvae, and single-celled organizms. Researchers have not emulated the full functionality of, for example, an elephant trunk, in the laboratory. However, the artificial designs to date do share several key features with their biological counterparts, including a significant transference of weight and complexity away from the actual manipulator. We refer to this design as "remote actuation" [9]; its benefits include a substantial reduction in design complexity and cost for manipulators such as the Clemson tentacle manipulator (Fig. 1) and the Rice/Clemson elephant's trunk manipulator [29]. Continuum robots also possess a useful characteristic termed *inherent compliance*. The infinite-dimensional kinematics of continuous "backbones" admit an infinity of possible backbone configurations for any given finite set of applied forces or torques along the backbone. Thus, such manipulators naturally comply with obstacles or nonconservative forces in a minimum-energy fashion. Properly controlled, this feature can eliminate the need for expensive and complex force-feedback mechanisms. In short, the preceding characteristics of hyper-redundant and continuum manipulators make them attractive for the kinds of tasks at which their biological counterparts excel: locomotion through highly cluttered areas, whole-arm manipulation, and a delicate natural compliance to the environment, for example.

Research into the characteristics and capabilities of continuum robotics necessitates an overall increase in the complexity of the manipulator kinematic and dynamic models. Serial, rigid-link robot kinematics essentially consist of algebraic-trigonometric descriptions, while continuum robot kinematics involve differential equations for all but the simplest cases. Rigid-link dynamics usually involve nonlinear ordinary differential equations, while continuum dynamics employ nonlinear partial differential equations.

Several researchers have addressed topics related to manipulation and locomotion using hyper-redundant and continuum robots. Among these, the pioneering work of Hirose [16] represents a large step forward in the realization of practical snake-like devices. Chirikjian and Mochiyama, [3]–[7], [21], [22] contribute to the theoretical development of hyper-redundant kinematics, path planning, and shape optimization; notably, [4] makes a quantitative comparison between the dynamics of hyper-redundant and continuum manipulators. Further work in kinematics, dynamics, control, and practical design considerations appear in [9]–[15], and [29]. Other trunk-like prototypes can be seen in [8] and [17]. Robinson and Davies [24] also provide a good overview of work in the area, and our previous work in [11] illustrates an application of the

I. A. Gravagne is with the Department of Engineering, Baylor University, Waco, TX 76798-7356 USA (e-mail: Ian_Gravagne@baylor.edu).

C. D. Rahn is with the Department of Mechanical and Nuclear Engineering, Pennsylvania State University, University Park, PA 16802 USA (e-mail: cdrahn@psu.edu).

I. D. Walker is with the Department of Electrical and Computer Engineering, Clemson University, Clemson, SC 29634 USA (e-mail: ianw@ces.clemson.edu).

concepts in this paper to the relatively simple, small-deflection dynamic rod model. A thorough discussion of vibration and noise-control techniques for distributed systems appears in [23]. On the specific subject of continuum manipulation, Wilson, *et al.* presented a series of works including a kinematic and dynamic analysis of planar manipulators with payload effects [27], [30], [31]; however, their work did not concentrate on control strategies and the dynamics formulations in this paper are significantly different and somewhat more general. Also of interest is the extensive work of Kier [18], detailing the physical structure of many animals that employ continuous manipulation techniques.

The objective of this work is to explore the dynamics of a simple planar continuum manipulator section, and to formulate a simple controller that achieves setpoint tracking while minimizing the incidental vibrations excited in the backbone. Several key features of this work make it unique: the use of a large-deflection dynamic model incorporating axial extensibility, the implementation of a controller that seeks to regulate the flexible body to a nonzero equilibrium and the use of cable tension coupling feedback in the control law. The specific geometry of the device under consideration in this work will be discussed shortly.

II. SPRING-STEEL MANIPULATOR

Fig. 1 illustrates the tentacle manipulator. The manipulator consists of two sections, each with two degrees of freedom (DOF). Its central backbone is a continuous elastic rod, with cable guides periodically spaced along its length. Four cable pairs run through the guide eyelets, two pairs terminating at the midpoint, and two at the endpoint. Through differential variation of the cable tensions, torques may be applied in orthogonal directions at the midpoint or endpoint of the backbone. Knowledge of how the rod kinematics respond to the application of such torques permits prediction of the robot's shape and endpoint coordinates. To maximize the workspace of the tentacle, the rod must be sufficiently long and thin to allow very large elastic, small strain displacements. Thus, sudden movements (whether by external forces or the intentional application of control torques) tend to excite undesirable vibrations in the rod. At best, these vibrations simply force the adoption of a "slower" trajectory; at worst they can destabilize the feedback controller guiding the robot's position.

Fortunately, friction between the cables and the cable guides introduces some vibration damping. As the backbone bends, friction between a cable and its guides increases on the concave side of the curve. However, cable-guide friction must be minimized to maximize the robot workspace and maintain tractable kinematics. Near the zero-stress configuration (a straight line in our case), the effects of cable friction are reduced because the cable tensions are small. In [11] we argue that this fact warrants the use of a small-deflection, linear dynamic rod model. The setpoint analysis in [11] is effective near the straight-line configuration, but the control strategy cannot be proven stable in the general case because large rod deflections violated the restrictions of the dynamic model.
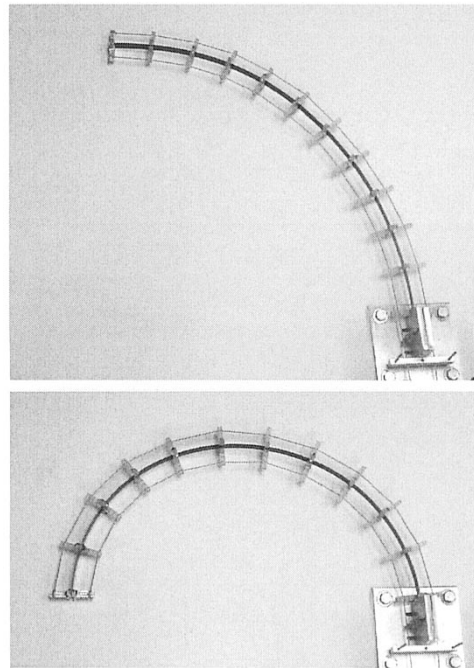

Fig. 2. Spring-steel backbone can bend in excess of 180°.

With appropriate assumptions and observations, the small-deflection rod decouples in orthogonal planes, allowing a discussion of the rod's behavior in three dimensions. No such decoupling occurs in the large-deflection case, so for simplicity we will restrict ourselves to a planar system. The experimental testbed for our work uses a backbone of spring steel, very wide relative to its thickness so that it only bends in one plane. Similar to the tentacle manipulator, the spring-steel backbone has a set of cable guides spaced along its length, with cables finally terminating at the distal end. The backbone can bend 180° and beyond (Fig. 2), clearly requiring the use of a large-deflection dynamic model; see Section IX for more details.

Additionally, we note that, even though this paper focuses on a planar model, the work here anticipates further study into the full three-dimensional (3-D) model. Consequently, we intentionally rule out sensor options which would be relatively simple to implement in the plane, if they will not also work in the spatial case. Such options include strain sensors on the flat side of the spring steel (such sensors could not be attached to a round backbone), position measurements using an overhead camera (which can only measure planar deflections), and shear sensors at the free boundary (due to weight constraints in the spatial case).

III. LARGE DEFLECTION DYNAMICS

The set $\mathcal{C}$ of allowable beam planar configurations contains the duples $\{\underline{x}(s), Q(s)\}$ where

$$\mathcal{C} = \left\{ \{\underline{x}(s), Q(s)\} \colon [0, L] \to \Re^2 \times SO(2) \right\}. \qquad (1)$$

The vector $\underline{x}(s)$ is the position of the beam centerline, $Q(s)$ is an orientation (i.e., rotation) matrix, s is an independent parameterization variable, and L is the beam length at rest. If the beam

is inextensible, s represents the arc length as measured from the origin. We include the effects of beam extensibility, so the set $\mathcal{C}$ is not strictly arc-length parameterized. Only under the special conditions of zero axial extension or contraction does s truly measure arc length. The subsequent analysis requires two mild conditions on the allowable configurations set.

1) Given the elementary basis vectors $\{\underline{e}_1, \underline{e}_2\}$ and the product $Q\underline{e}_i \triangleq \underline{q}_i(s)$, we assume that

$$\underline{x}'(s) \cdot \underline{q}_1(s) > 0 \tag{2}$$

where $\underline{x}' \triangleq \partial \underline{x}/\partial s$.

2) Given the energy in the rod in the form $E = \int_0^L f(s)\,ds + \sum_j g(s_j)$ for $0 \le s_j \le L$, we assume

$$E < \infty \Rightarrow f(s) \in \mathcal{L}^\infty \tag{3}$$

where $f(s) \ge 0$ represents the deformation energy density of the rod, $g(s_j) > 0$ represents lumped-parameter energy stored in point masses and springs, and $f(s) \in \mathcal{L}^\infty$ means $|f(s)| < \infty$ for all $s \in [0, L]$.

Condition 1) states that the beam may not experience infinite shear stress, for reasons which will become clearer later. For condition 2), we assume that "Dirac delta" distributions in the energy functional $f(s)$ are disallowed; intuitively, this implies that the rod cannot experience single-point changes in distributed coordinates such as curvatures or positions. Condition 2) does not arise from strictly mathematical arguments; it simply states a physically reasonable assumption motivated by engineering judgement.

A. Energy Formulations

For beams with high aspect ratios (length to thickness), potential energy can be stored via three basic types of elastic deformations: bending, axial and shear. For a beam of cross-sectional area A, cross-sectional moment of inertia I, Young's modulus E and shear modulus G, each elastic deformation has an associated stiffness. The product EI is the bending stiffness, EA is the axial stiffness, and GA is the shear stiffness. (We assume that the effective shear area equals the cross-sectional area, for simplicity.)

Fig. 3 illustrates the difference between shear and bending deformations, in the case that there is no axial compression or tension. Note that, in case a), the orientation vector $\underline{q}_1$ does not vary along the length of the beam. The beam has been divided into (infinitesimally) small segments, and Q reflects the orientation of each segment. Thus, a good measure of the axial and shear "stretch" of each segment would be the difference of the tangent vector and the principal orientation vector, i.e., $\underline{v} = (\underline{x}' - \underline{q}_1)$. Applying Hooke's Law, the resultant deformation energies for that segment would be $(1/2)EAv_1^2$ plus $(1/2)GAv_2^2$, or simply $(1/2)\underline{v}^T C\underline{v}$, where $C = \text{diag}\{EA, GA\}$. To generalize this initial formulation, imagine that the columns of C represent the principal axes of a stiffness ellipsoid centered around the segment. As the orientation of a segment changes, the ellipsoid rotates also, to keep the principal axes properly aligned. A simple similarity transformation will accomplish this rotation, so that shear/axial energy for that segment becomes $(1/2)\underline{v}^T QCQ^T \underline{v}$.
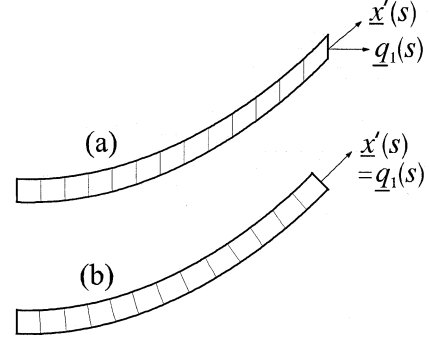

Fig. 3. Beam in (a) experiences significant shear deformations, but no bending. Conversely, in (b) shear effects are not present. Note that the curve tangent is the same in both cases.
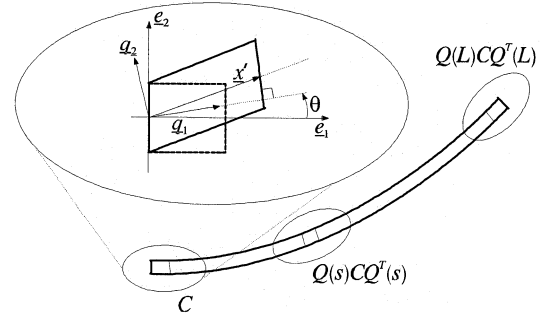

Fig. 4. Illustration of a small beam segment experiencing axial, shear, and flexural deformation. Note how the stiffness ellipsoid changes orientation along the length of the beam.

This is illustrated in the close-up of Fig. 4. "Adding up" the segment energies gives the potential energy

$$PE = \frac{1}{2} \int_0^L \left\{ \frac{1}{2} \underline{v}^T QCQ^T \underline{v} + EI\theta'^2 \right\} ds. \tag{4}$$

The kinetic energy is more straightforward. We simply endow each quantity above with a time dependency, and sum the kinetic energies of each infinitesimal segment to get

$$KE = \frac{1}{2} \int_0^L \left\{ \rho_m \|\underline{\dot{x}}(s, t)\|^2 + \rho_j \dot{\theta}(s, t)^2 \right\} ds \tag{5}$$

where ρ_m is the mass density of the beam, and ρ_j is the angular inertia density.

B. Dynamics Formulation

The preceding energy functionals appear in different forms in [25] and in [26]. In order to apply Hamilton's principle to the energy expressions above, we first formulate the work due to the application of tension to the cables on the beam. As the beam bends, the cable tension $F(t)$ induces both shear forces (perpendicular to the backbone centerline) and moments at the points where the cable passes through a guide standoff. As shown in [19], standoffs of the correct dimension and quantity can minimize the effect of the intermediate shears and moments along the backbone relative to the boundary moment at the terminal standoff. Consequently, we may formulate a simple
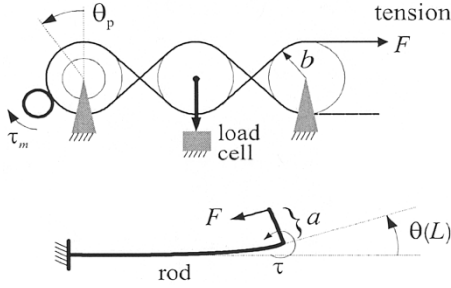
Fig. 5. Illustration of the various geometric quantities in the cable/pulley system.

external work function dependent only upon the boundary moment $\tau(t) = aF(t)$

$$W = \tau(t)\theta(L). \tag{6}$$

Applying Hamilton's principle to the expressions for KE, PE, and W yields the resulting dynamical equations and boundary conditions

$$\rho_m \underline{\ddot{x}} - \left[QCQ^T\underline{v}\right]' = \underline{0} \tag{7a}$$

$$\rho_j \ddot{\theta} - EI\theta'' - \underline{x}'^T SQCQ^T\underline{v} = 0 \tag{7b}$$

$$EI\theta'(L, t) = \tau(t) \tag{7c}$$

$$QCQ^T\underline{v}|_L = \underline{0} \tag{7d}$$

$$\theta(0, t) = 0 \tag{7e}$$

$$\underline{x}(0, t) = \underline{0} \tag{7f}$$

where S is the skew-symmetric matrix

$$S = \begin{bmatrix} 0 & 1 \\ -1 & 0 \end{bmatrix}. \tag{8}$$

The boundary conditions in (7d) reveal the absence of applied axial or shear forces on the free end of the beam; (7e) and (7f) indicate that the beam is clamped at the origin. We stress that these dynamics, along with the following analysis, applies only to one section of a continuum robot; we do not address the challenges associated with multiple-section dynamics here.

A deeper and more general dynamic analysis of large deflection planar beams appears in [26].

IV. BOUNDARY TORQUE DAMPER

As illustrated in Fig. 5, the control cables attach to a pulley of radius b, driven by a motor through a gear ratio of $r \gg 1$. The angle of the motor is θ_m and the angle of the pulley is θ_p. Given that the motor has rotational inertia J and viscous friction B, we may take the simple motor model

$$J\ddot{\theta}_m + B\dot{\theta}_m + \tau_p = \tau_m \tag{9}$$

where $\tau_p = (b/r)F$ is the torque due to the cable tension F, and τ_m the applied motor torque. Note the geometric relationship between the motor angle, the pulley angle and the backbone boundary angle

$$\theta_m = r\theta_p = \frac{ra}{b}\theta(L, t) \tag{10}$$

so that (9) becomes

$$J\frac{ra}{b}\ddot{\theta}(L, t) + B\frac{ra}{b}\dot{\theta}(L, t) + \frac{b}{r}F = \tau_m. \tag{11}$$

We choose the feedback control law

$$\tau_m = -k_p\tilde{\theta}(L, t) - k_d\dot{\theta}(L, t) - k_cF \tag{12}$$

where $\tilde{\theta}(L, t) = \theta(L, t) - \theta_d$ with $k_p, k_d, k_c > 0$, and θ_d is the desired boundary angle setpoint. Substituting (12) back into (11) and solving for F produces boundary torque

$$\tau = aF = -J_{\text{eff}}\ddot{\theta}(L, t) - K_d\dot{\theta}(L, t) - K_p\tilde{\theta}(L, t) \tag{13}$$

with

$$K_d = \left[\frac{Br\frac{a^2}{b} + ak_d}{k_c + \frac{b}{r}}\right] \quad K_p = \left[\frac{ak_p}{k_c + \frac{b}{r}}\right] \quad J_{\text{eff}} = \left[\frac{Jr\frac{a^2}{b}}{k_c + \frac{b}{r}}\right]. \tag{14}$$

Because of the relatively high gear ratio r required to bend the rod, (11) suggests that the motor will feel little of the back-driving effect of the rod dynamics transmitted though the cable tension F. The coupling factor k_c increases the effective back-driveability of the motor/gear system, providing greater control over the rod boundary. Associating (13) with (7c) results in the new boundary condition

$$EI\theta'(L, t) + J_{\text{eff}}\ddot{\theta}(L, t) = -K_d\dot{\theta}(L, t) - K_p\tilde{\theta}(L, t). \tag{15}$$

(Remark: We have implied that F is bipolar [a positive or negative quantity], but a cable can only support tension. The "tension" F really is the subtraction of the two tensions of an opposing cable pair. This subtraction is performed mechanically, as in Fig. 5, and without loss of generality we continue to refer to F simply as the cable tension.)

V. CONTROLLER STABILITY

The stability proof for the control system employs an energy-based Lyapunov functional, consisting of both the distributed energies of (5) and (4), and two lumped-parameter energies.

$$V = KE + PE + \frac{1}{2}K_P\tilde{\theta}(L, t)^2 + \frac{1}{2}J_{\text{eff}}\dot{\theta}(L, t)^2. \tag{16}$$

The first lumped-parameter represents a virtual torsional spring, attached to the free boundary with spring constant K_P. The second represents the effect of the motor and gear inertias. After some calculation, the power flow from the system is

$$\dot{V} = -K_d\dot{\theta}(L, t)^2 \tag{17}$$

which is negative semidefinite, proving system stability.

Note that, since we know above that $V < \infty$, then, it follows that $(1/2)\int_0^L EI\theta'^2\,ds < \infty$. Invoking Condition 2 from Section III implies that $\theta'^2(s, t) \in \mathcal{L}^\infty$, which in turn implies that $|\theta'(L, t)| < \infty$. Using boundary condition (7c), we see that $|\tau| < \infty$, so that $|F| < \infty$. Similarly, from the Lyapunov result, it follows that $|\tilde{\theta}(L, t)| < \infty$ and $|\dot{\theta}(L, t)| < \infty$. Consequently, the control (12) law must be composed of signals which are all bounded.

We reach a similar conclusion in [11], and then proceed to use an invariance principle to prove that, if $\dot{\theta}(L, t) \equiv 0$, then, the only allowable rod configuration was the static equilibrium solution. However, the simple nature of the linear model used there makes an asymptotic convergence proof possible, primarily due to separability. On the other hand, the current dynamical model is highly nonlinear and significantly more detailed, casting doubt on even the existence of an asymptotic convergence result. In a continuous elastic system, the possibility exists that a given control scheme or system configuration might isolate certain vibrational modes. In that case, energy would remain "trapped" in the system, possibly disallowing convergence of the system to the control objective. Specifically, (17) seems to indicate that modes for which $\dot{\theta}(L, t) = 0$ are uncontrollable. In order to address this possibility, we observe that we may derive a good approximation of the system motion by linearizing the dynamics about the beam's static equilibrium. This is the objective of the following two sections.

VI. EQUILIBRIUM IN THE BEAM

If we neglect all time-derivative terms, the first field equation (7a) suggests that the shear and axial forces must be constant, i.e., $QCQ^T \underline{v} = \underline{c}$. But boundary condition $QCQ^T \underline{v}|_L = \underline{0}$ shows that $\underline{c} = \underline{0}$. Since QCQ^T is always full rank, this must mean that $\underline{v}(s) = 0$, or

$$x_1' = \cos(\theta)$$
$$x_2' = \sin(\theta). \qquad (18)$$

Therefore, the second field equation simplifies to

$$\theta'' = 0 \qquad (19)$$

supporting from first principles the constant curvature formulas found in [9]–[15].

We next dissect the solutions for θ, x_1, and x_2 into their static and dynamic components

$$\theta(s, t) = \overline{\theta}(s) + \hat{\theta}(s, t)$$
$$x_i(s, t) = \overline{x}_i(s) + \hat{x}_i(s, t) \qquad (20)$$

where $\overline{\theta}$ and $\overline{x}_i$ are the spatial equilibrium solutions, and $\hat{\theta}$ and $\hat{x}_i$ are the time-varying dynamic coordinates. Thus, (18) and (19) become

$$\overline{\theta}'' = 0 \qquad (21)$$
$$\overline{x}_1' = \cos(\overline{\theta}) \quad \overline{x}_2' = \sin(\overline{\theta}) \qquad (22)$$

which implies

$$\overline{\theta}(s) = \kappa s \qquad (23)$$
$$\overline{x}_1'(s) = \cos(\overline{\theta}) \quad \overline{x}_2'(s) = \sin(\overline{\theta}) \qquad (24)$$
$$\overline{x}_1(s) = \frac{1}{\kappa} \sin(\overline{\theta}) \quad \overline{x}_2(s) = \frac{1}{\kappa} \left(1 - \cos(\overline{\theta})\right) \qquad (25)$$

accounting for the geometric boundary conditions. Note the similarity of these expressions to the analogous ones in [6]. Thus, the equilibrium shape is a circular arc. (Note that $\overline{x}_1$ and $\overline{x}_2$ always exist even in the case of zero curvature, $\kappa = 0$.)

Using these equilibrium equations, along with boundary condition (15), we find that the steady-state error for the system is

$$\tilde{\theta}(L) = \frac{-\theta_d}{1 + K_p \left(\frac{L}{EI}\right)} \qquad (26)$$

which can be arbitrarily reduced by increasing K_p, an intuitive result.

VII. LINEARIZATION PROCEDURE

The dynamic variables remain unknown, but we next assume that their range is a "small" neighborhood around the origin. This being the case, we linearize the dynamics and boundary conditions about the equilibrium by evaluating a first-order Taylor expansion about $\overline{\theta}$ and $\overline{x}$

$$\underline{f}(\underline{z}) \cong \underline{f}(\overline{z}) + \left[\frac{\partial \underline{f}}{\partial \underline{z}}\right]_{\overline{z}} \hat{\underline{z}}$$

where the coordinate vector $\underline{z}$ is

$$\underline{z} = \begin{bmatrix} \theta & x_1 & x_2 & \dot{\theta} & \dot{x}_1 & \dot{x}_2 & \ddot{\theta} & \ddot{x}_1 & \ddot{x}_2 \\ \theta' & x_1' & x_2' & \theta'' & x_1'' & x_2'' \end{bmatrix}^T$$

and

$$\underline{f}(\underline{z}) = \begin{bmatrix} \rho_j \ddot{\theta} - EI\theta'' - \underline{x}'^T SQCQ^T \underline{v} \\ \rho_m \ddot{\underline{x}} - \left(QCQ^T \underline{v}\right)' \end{bmatrix} = \underline{0}. \qquad (27)$$

The equilibrium vector will be

$$\overline{z} = \begin{bmatrix} \overline{\theta} & \overline{x}_1 & \overline{x}_2 & 0 & 0 & 0 & 0 & 0 & 0 \\ & \overline{\theta}' & \overline{x}_1' & \overline{x}_2' & 0 & \overline{x}_1'' & \overline{x}_2'' \end{bmatrix}^T$$

because $\overline{\theta}'' = 0$ and all time-derivatives are zero by definition. As expected, $\underline{f}(\overline{z}) = 0$ by direct calculation, simplifying with (23) and (24). Thus, evaluating the Taylor expansion yields

$$\left[\frac{\partial \underline{f}}{\partial \underline{z}}\right]_{\overline{z}} \hat{\underline{z}} = \begin{bmatrix} \rho_j \ddot{\hat{\theta}} - EI\hat{\theta}'' + GA\hat{\theta} - GA\overline{x}'^T S\hat{x}' \\ \rho_m \ddot{\hat{x}} - \left(\overline{Q}C\overline{Q}^T \hat{x}'\right)' + GA\left(S^T \overline{x}'\hat{\theta}\right)' \end{bmatrix} = \underline{0} \qquad (28)$$

a nonsingular expression, linear in the "hat" variables. The associated boundary conditions are

$$EI\hat{\theta}'(L, t) = -J_{\text{eff}}\ddot{\hat{\theta}}(L, t) - K_d\dot{\hat{\theta}}(L, t)$$
$$\qquad\qquad - K_p\hat{\theta}(L, t) \qquad (29)$$
$$\hat{\underline{x}}'(L, t) = S^T \overline{x}'\hat{\theta}(L, t) \qquad (30)$$
$$\hat{\theta}(0, t) = 0 \qquad (31)$$
$$\hat{\underline{x}}(0, t) = \underline{0}. \qquad (32)$$

We next apply LaSalle's Invariance Principle to the linearized dynamics, analyzing the possible system solutions if $\dot{V} \equiv 0$, implying $\dot{\hat{\theta}}(L, t) \equiv 0$ and $\hat{\theta}(L, t) \equiv 0$. Furthermore, we assume that the linearized system may be spatially and temporally separated, so that

$$\hat{\theta} = \Theta(s)W(t)$$
$$\hat{\underline{x}} = \underline{X}(s)W(t). \qquad (33)$$

From the Lyapunov argument, we know that the sum of all vibrational modes must be stable, so without loss of generality we may analyze the system one mode at a time, by assigning $W(t) = \exp(j\omega t)$. The common temporal term can now be factored out of the dynamics and boundary conditions, leaving

$$
\begin{aligned}
\left(GA - \rho_j \omega^2\right)\Theta - EI\Theta'' \\
+ GA\underline{\overline{x}}'^T S \underline{X}' = 0
\end{aligned}
\tag{34a}
$$

$$
\begin{aligned}
-\rho_m \omega^2 \underline{X} - \left(\overline{Q}C\overline{Q}^T \underline{X}'\right)' \\
+ GA\left(S^T \underline{\overline{x}}'\Theta\right)' = \underline{0}
\end{aligned}
\tag{34b}
$$

$$
EI\Theta'(L) = -K_p \Theta(L)
\tag{34c}
$$

$$
\underline{X}'(L) = S^T \underline{\overline{x}}'\Theta(L)
\tag{34d}
$$

$$
\Theta(0) = 0
\tag{34e}
$$

$$
\underline{X}(0) = \underline{0}.
\tag{34f}
$$

Consequently, the requirement $\dot{\hat{\theta}}(L, t) = \Theta(L)\dot{W}(t) \equiv 0$ occurs in two cases.

Case 1, $\omega \equiv 0$: The solution of (34) is $\Theta(s) = 0$ and $\underline{X}(s) = \underline{0}$. The beam equilibrium shape is then the largest invariant set containing $\dot{V} \equiv 0$, so LaSalle's invariance principle proves that the origin is asymptotically stable.

Case 2, $\Theta(L) \equiv 0$: This case can be thought of as an additional boundary condition, bringing the list of boundary conditions to

$$
\Theta(L) = 0 \quad \Theta'(L) = 0 \quad \underline{X}'(L) = 0
\tag{35a}
$$

$$
\Theta(0) = 0 \quad \underline{X}(0) = 0.
\tag{35b}
$$

Unfortunately, the associated boundary value problem is highly coupled and does not lend itself to closed-form analysis. Also, neither boundary supports enough conditions to numerically integrate a solution. The free boundary has the most conditions, so we now set the condition for $\underline{X}(L)$ in two separate cases. For each instance, we label the associated solutions as

$$
\underline{X}(L) = \begin{bmatrix} 1 \\ 0 \end{bmatrix} \longmapsto \left\{\Theta^{(1)}(s), \underline{X}^{(1)}(s)\right\}
\tag{36}
$$

$$
\underline{X}(L) = \begin{bmatrix} 0 \\ 1 \end{bmatrix} \longmapsto \left\{\Theta^{(2)}(s), \underline{X}^{(2)}(s)\right\}.
\tag{37}
$$

With six final conditions in expressions (35a) and either (36) or (37), we can integrate backward to $s = 0$, noting that the integration must also satisfy the initial conditions in (35b). From linearity, we have

$$
\underline{X}(L) = \alpha\begin{bmatrix} 1 \\ 0 \end{bmatrix} + \beta\begin{bmatrix} 0 \\ 1 \end{bmatrix} \longmapsto \left\{\begin{aligned} \Theta(s) &= \alpha\Theta^{(1)}(s) + \beta\Theta^{(2)}(s) \\ \underline{X}(s) &= \alpha\underline{X}^{(1)}(s) + \beta\underline{X}^{(2)}(s) \end{aligned}\right\}
\tag{38}
$$

by superposition. The boundary conditions at the clamped end of the beam must still hold, implying

$$
M\begin{bmatrix} \alpha \\ \beta \end{bmatrix} \triangleq \begin{bmatrix} \Theta^{(1)}(0) & \Theta^{(2)}(0) \\ \underline{X}^{(1)}(0) & \underline{X}^{(2)}(0) \end{bmatrix}\begin{bmatrix} \alpha \\ \beta \end{bmatrix} = \underline{0} \quad M \in \Re^{3\times 2}
\tag{39}
$$

for arbitrary frequency ω. If M has full rank for all ω, then the only solution to (39) would be $\alpha = \beta = 0$. This would imply that the only valid free boundary position is $\underline{X}(L) = \underline{0}$.

Numerically integrating (34a) and (34b) with (35a) and $\underline{X}(L) = \underline{0}$ yields $\underline{X}(s) = \underline{0}$ and $\Theta(s) = 0$. Therefore, in the case that $\text{rank}(M) = 2$ we may again invoke LaSalle's Invariance Principle to show that the beam will asymptotically converge to its equilibrium point. However, we find that M does not always have full rank. The next section explores this observation.

VIII. AXIAL/SHEAR VIBRATIONS

Consider the case of a straight-line equilibrium shape with zero curvature. Now $\overline{\theta} = 0$ and $\underline{\overline{x}}' = [1, 0]^T$ so (28) becomes

$$
\rho_j\ddot{\hat{\theta}} - EI\hat{\theta}'' + GA\hat{\theta} - GA\hat{x}_2' = 0
\tag{40a}
$$

$$
\begin{bmatrix} \rho_m\ddot{\hat{x}}_1 - EA\hat{x}_1'' \\ \rho_m\ddot{\hat{x}}_2 - GA\hat{x}_2'' + GA\hat{\theta}' \end{bmatrix} = \underline{0}.
\tag{40b}
$$

The first expression in (40b) is simply the wave equation, governing the dynamics of axial vibrations in the beam. The boundary conditions from (30) and (32) are $\hat{x}_1'(L, t) = 0$ and $\hat{x}_1(0, t) = 0$. Clearly, if there is any initial axial endpoint displacement, $\hat{x}_1(L, t) \neq 0$, these dynamics will advance unhindered by any dissipative reaction from the controller. The axial motion decouples from the transverse motion, so the controller provides no axial damping. The frequencies of vibration are

$$
\omega_{\text{axial}} = \frac{(2n+1)\pi}{L}\sqrt{\frac{EA}{\rho_m}}, \qquad n = 0, 1, 2\ldots.
\tag{41}
$$

Numerical integration verifies these frequencies correspond to cases where $\text{rank}(M) < 2$. Furthermore, the simulations indicate that ω_{axial} remains fixed regardless of equilibrium curvature.

Now, consider the possibility that the beam's material and dimensions permit $EI \gg GA$ (by which we mean at least an order of magnitude larger). Generally, $\rho_m \gg \rho_j$, so equation (40a) would render the quantities $GA\hat{\theta}$ and $GA\hat{\theta}'$ relatively small compared with $GA\hat{x}_2''$. Consequently, the second expression in (40b) would be $\rho_m\ddot{\hat{x}}_2 - GA\hat{x}_2'' \approx 0$. As long as GA and EI remain nonzero, this expression will always remain coupled with (40a), and the boundary torque damper. Nevertheless, this "thick" beam may exhibit shear vibrations requiring a long time to damp out. Their frequencies are

$$
\omega_{\text{shear}} = \frac{(2n+1)\pi}{L}\sqrt{\frac{GA}{\rho_m}}, \qquad n = 0, 1, 2\ldots.
\tag{42}
$$

We note that carrying out a numerical integration in (34a) and (34b) requires the definition of the constants EI, EA, GA, ρ_m, ρ_j, and L. While the integration should produce consistent results with virtually arbitrary (nonzero) choices of these constants, a great deal of effort may be expended attempting to interpret results corresponding to constants that cannot physically attain the chosen values. For instance, G and E are related through Poisson's ratio υ as
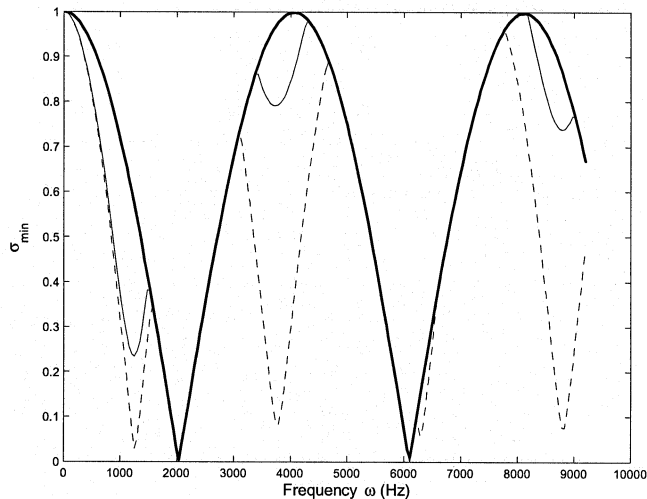
$$
G = \frac{E}{2 + 2\upsilon}.
$$

Fig. 6. Minimum singular value $\sigma_{\min}$ of M versus frequency ω. Bold line represents the spring-steel backbone. Thin and dotted lines are for $EI = GA$ and $EI = 10GA$, respectively.
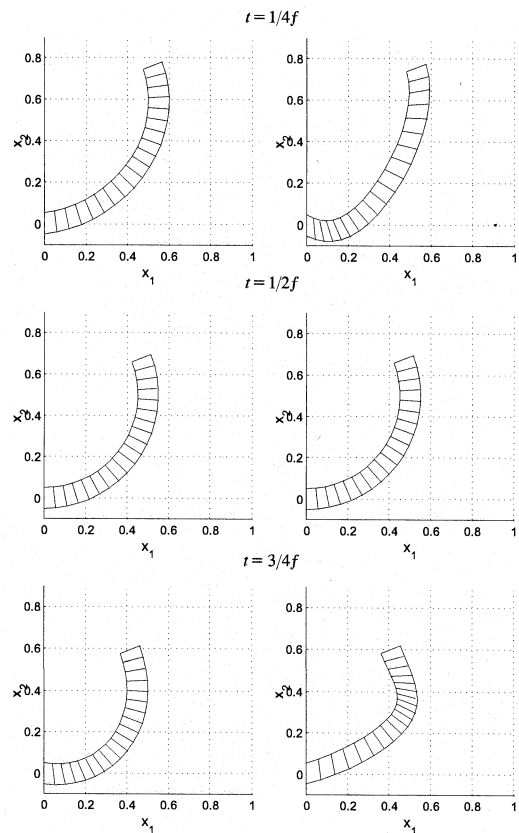

Fig. 7. Left and right columns represent the first and second modes of axial vibration about a nonzero equilibrium curvature, respectively. Note the semicircular equilibrium shape in the middle frame, and $f = 2\pi\omega_{\mathrm{axial}}$.

Since $v \in [0.2, 0.6]$ for nearly all solid materials, this places a fairly tight restraint on the value of the shear modulus relative to Young's modulus. Similarly, the elastic, small-strain energy formulations used to derive the dynamics assume a large beam aspect ratio (a beam with a high length-to-thickness ratio). Consequently, it will usually be found that $\rho_j \ll \rho_m$. However, even within the constraint of a large aspect ratio, it is possible for EI to vary, over several orders of magnitude, a possibility with interesting implications mentioned above.

For the spring-steel robot, the constants used in the numerical simulation were based partly on measurements, and partly on material data available from a variety of sources. The calculations of constants ρ_j and I depend on the cross-sectional shape of the beam; see [20] and [26] for more detail. Using $L = 0.64$ m, $E = 2 \times 10^{11}$ N/m², $v = 0.3$, $A = 10.5 \times 10^{-6}$ m², $\rho_m = 0.0781$ kg/m, $\rho_j = 4.485 \times 10^{-9}$ kg·m, and $I = 6.05 \times 10^{-13}$ m⁴, a plot of the minimum singular value $\sigma_{\min}$ of M, versus frequency ω appears in Fig. 6. The bold line, reflecting simulation results using these constants, indicates allowable frequencies at the predicted values of ω_{axial}. The thin line in Fig. 6 represents the behavior of $\sigma_{\min}$ if $EI \simeq GA$. The dotted line shows the same plot for $EI \simeq 10GA$. Note the presence of large dips corresponding exactly to the frequencies of ω_{shear}. Images of the first and second modes of axial vibration, with curvature $\kappa = 2$, appear in Fig. 7. Note that the endpoint slope $\Theta(L)$ remains fixed throughout the motion so rotary endpoint damping has no effect on these modes.

IX. EXPERIMENTAL SETUP AND RESULTS

The experimental spring steel backbone, illustrated back in Fig. 2, is 64-cm long, 0.8-mm thick, and 1.27-cm wide. The cables are suspended 1.27 cm from the beam centerline, and threaded through 11 cable standoffs. The main drawback to cable designs centers on the problem of friction in the cable standoffs, a phenomenon not modeled here. As the cable tensions rise to overcome stiffness while the robot bends, friction

at the pass-through points becomes a more severe problem. In practice, this problem does not seriously hamper normal operation of manipulator until the backbone reaches curvatures at or near the recoverable surface strain limits of the material (around 1% for spring steels), but nevertheless efforts were made to reduce its effect by flaring the pass-through holes and using teflon-coated cables woven from very fine steel stands.

A picture of the tension-feedback load cell appears in Fig. 8. Because the application in this paper involves high-gain tension feedback, a piezo-based load cell was chosen to measure tension owing to its extremely clean and noise-free output as well as simplicity of use (relative to such technologies as strain gauges). The fact that piezo load cells are fundamentally dynamic sensors did not prove problematic because the particular load cells chosen have time constants of well over 60 s, meaning that for all practical purposes they yield "static" outputs for durations of 10 s or less and are more than capable of capturing the lowest frequency dynamics of the spring steel backbone.

The system was operated by a Pentium IV 400 MHz PC running Microsoft Windows NT 4 in conjunction with the real-time micro-kernel HyperKernel (Nematron, Inc.) through a Quanser MultiQ II I/O card.

The analysis shows that, if there is a nonzero initial shear or axial displacement on the beam, the torque-damper controller will drive the endpoint angle to a desired value, but not of the endpoint position. For thin beams, however, the axial and shear vibrations occur at high frequencies and with small amplitudes,
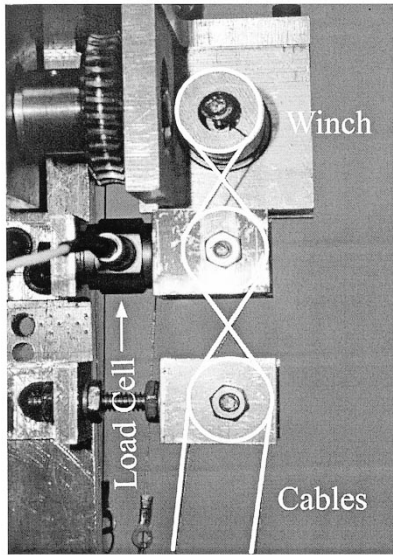
Fig. 8. Differential tension load cell system. Cables, pulleys, and winch are emphasized in white.
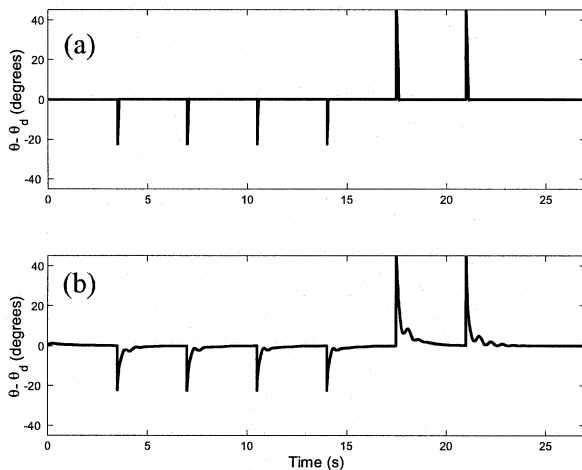

Fig. 9. Endpoint angle error response $\theta(t) - \theta_d$. (a) Without coupling, $k_c = 0$, $k_d = 0$. (b) With coupling, $k_c = 6$, $k_d = 0.025$

Fig. 10. Differential cable tension for the cases with and without coupling. Thin line: $k_c = 0$, $k_d = 0$. Thick line: $k_c = 6$, $k_d = 0.025$.

X. CONCLUSION

To summarize, we have taken an in-depth look at the dynamics of a single section of a planar, continuum robot backbone simply consisting of a thin elastic beam. Using an appropriate large-deflection dynamic model, we applied a PD-plus-coupling setpoint control strategy to attempt to damp out flexural vibrations near the origin as much as possible. An energy-based stability proof guaranteed the global stability of the controller. Also, we illustrated that asymptotic convergence of beam orientation and position is not possible in the presence of axial vibrations; however numerical estimates of the frequencies of those vibrations render them relatively benign. Experimental results on a backbone section made of highly elastic spring steel illustrated the efficacy of the control strategy.

Much work remains in the modeling, design, and characterization of continuum backbones. Clearly, a useful continuum manipulator consists of multiple sections serially connected, increasing the complexity of the model, as seen in [12], [13]. Dynamic and kinematic modeling in the general 3-D case presents a challenge also. Axial motions, while not practically problematic for a backbone of high axial stiffness, may in fact be highly desirable for manipulators which can contract and extend. One design has already been built with this capability [17], and with appropriate actuation the results in this paper could be extended to that case. From a sensing and actuation point of view, the possibility of using continuous actuation materials (e.g., "smart materials") exists [1], and the problem of obtaining straightforward curvature or position measurements for 3-D backbone curves persists. Nevertheless, the field of continuum and hyper-redundant manipulation holds great promise in both the theoretical and experimental domains.

rendering them insignificant compared with the bending motions. The coupling strategy of the controller trades slower angle convergence for faster position convergence, as illustrated in Fig. 9 where the beam angle steps over four 22.5° increments up to 90°, and then back to zero in two 45° increments. In Fig. 8(a) the angle error converges quickly to zero under proportional-derivative (PD) control. Adding coupling in Fig. 8(b) slows the angle transient, allowing the controller to extract energy from the system through the rotary angle motions. The manipulator does not have an endpoint position measurement sensor, but the differential tension measurement reflects the relative magnitude and duration of flexural vibrations in the beam. Fig. 10 shows the tension as the beam angle returns to the origin in the last step of Fig. 9. The presence of coupling along with a slight increase in overall damping significantly improves the vibrational characteristics of the beam's step response. As expected, the step back to the zero angle produced the worst vibrations, owing to the absence of cable friction at the origin.
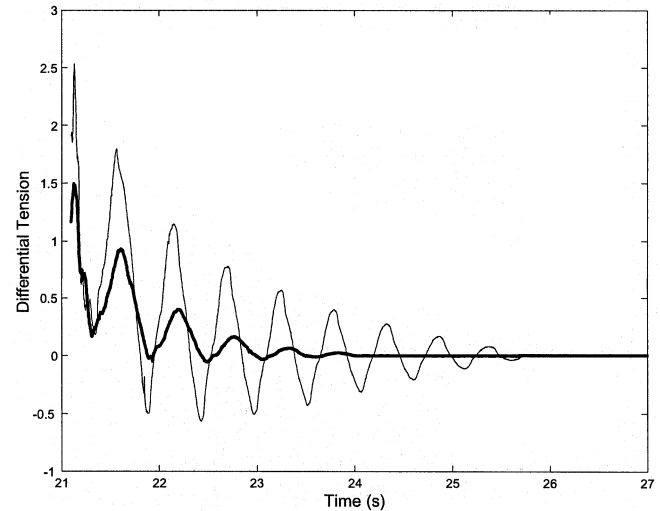
REFERENCES

[1] W. M. Aguilera and M. I. Frecker, "Design and modeling of an active steerable end-effector," in *Proc. SPIE Smart Structures and Materials: Modeling, Signal Processing and Control in Smart Stuctures*, vol. 4326, 2001, pp. 490–498.

[2] S. E. Burke and J. E. Hubbard, "Distributed actuator control design for flexible beams," *Automatica*, vol. 24, no. 5, pp. 619–627, 1988.

[3] G. S. Chirikjian, "Design and analysis of some nonanthropomorphic, biologically inspired robots: An overview," *J. Robot. Syst.*, vol. 18, no. 12, pp. 701–713, 2001.

[4] ——, "Hyper-redundant manipulator dynamics—A continuum approximation," *J. Adv. Robot.*, vol. 9, no. 3, pp. 217–243, 1995.

[5] G. S. Chirikjian and J. W. Burdick, "Kinematically optimal hyper-redundant manipulator configurations," *IEEE Trans. Robot. Automat.*, vol. 11, pp. 794–805, Dec. 1995.

[6] ——, "A modal approach to hyper-redundant manipulator kinematics," *IEEE Trans. Robot. Automat.*, vol. 10, pp. 343–354, June 1994.

[7] G. S. Chirikjian, "Theory and applications of hyper-redundant robotic manipulators," Ph.D. dissertation, Dept. of Appl. Mech., California Inst. of Technol., Pasadena, CA, June 1992.

[8] R. Cieslak and A. Morecki, "Elephant trunk type elastic manipulator—A tool for bulk and liquid materials transportation," *Robotica*, vol. 17, pp. 11–16, 1999.

[9] I. Gravagne and I. D. Walker, "Kinematic transformations for remotely-actuated planar continuum robots," in *Proc. IEEE Int. Conf. Robotics and Automation (ICRA)*, San Francisco, CA, May 2000, pp. 19–26.

[10] ——, "On the kinematics of remotely-actuated continuum robots," in *Proc. IEEE Int. Conf. Robotics and Automation (ICRA)*, San Francisco, CA, May 2000, pp. 2544–2550.

[11] I. Gravagne, C. D. Rahn, and I. D. Walker, "Good vibrations: A vibration damping setpoint controller for continuum robots," in *Proc. IEEE Int. Conf. Robotics and Automation (ICRA)*, Seoul, Korea, May 2001, pp. 3877–3884.

[12] I. Gravagne and I. D. Walker, "Manipulability, force and compliance analysis for planar continuum manipulators," *IEEE Trans. Robot. Automat.*, vol. 18, pp. 263–273, June 2002.

[13] ——, "Uniform regulation of a multi-section continuum manipulator," in *Proc. IEEE Int. Conf. Robotics Automation (ICRA)*, Washington, DC, May 2002, pp. 1519–1524.

[14] M. Hannan and I. D. Walker, "Novel kinematics for continuum robots," in *Proc. 7th Int. Symp. Advances in Robot Kinematics*, Piran, Slovenia, June 2000, pp. 227–238.

[15] ——, "Analysis and initial experiments for a novel elephant's trunk robot," in *Proc. Int. Conf. on Intelligent Robots and System (IROS)*, Takamatsu, Japan, Nov. 2000, pp. 330–337.

[16] S. Hirose, *Biologically Inspired Robots*. Oxford, U.K.: Oxford Univ. Press, 1993.

[17] G. Immega and K. Antonelli, "The KSI tentacle manipulator," in *Proc. IEEE Int. Conf. Robotics and Automation (ICRA)*, Nagoya, Japan, May 1995, pp. 3149–3154.

[18] W. M. Kier and K. K. Smith, "Tonques, tentacles and trunks—The biomechanics of movement in muscular hydrostats," *Zoo. J. Linnean Society*, vol. 83, no. 4, pp. 307–324, 1985.

[19] C. Li and C. D. Rahn, "Design of continuous backbone, cable-driven robots," *J. Mech. Des.*, vol. 124, pp. 256–271, 2002.

[20] E. H. Love, *A Treatise on the Mathematical Theory of Elasticity*. New York: Dover, 1944.

[21] H. Mochiyama and H. Kobayashi, "The shape Jacobian of a manipulator with hyper degrees of freedom," in *Proc. IEEE Int. Conf. Robotics and Automation (ICRA)*, Detroit, MI, May 1999, pp. 2837–2842.

[22] ——, "Shape correspondence between a spatial curve and a manipulator with hyper degrees of freedom," in *Proc. IEEE/RSJ Int. Conf. Intelligent Robots and Systems (IROS)*, Victoria, BC, Canada, Oct. 1998, pp. 161–166.

[23] C. D. Rahn, *Mechatronic Control of Distributed Vibration and Noise*. Berlin, Germany: Springer-Verlag, 2001.

[24] G. Robinson and J. B. C. Davies, "Continuum robots—A state of the art," in *Proc. IEEE Int. Conf. Robotics and Automation (ICRA)*, Detroit, MI, May 1999, pp. 2849–2854.

[25] J. C. Simo, N. Tarnow, and M. Doblare, "Non-linear dynamics of three-dimensional rods: Exact energy and momentum conserving algorithms," *Int. J. Numer. Methods Eng.*, vol. 38, pp. 1431–1473, 1995.

[26] J. C. Simo and L. Vu-Quoc, "On the dynamics of flexible beams under large overall motions—The plane case," *ASME J. App. Mech.*, vol. 53, no. 4, pp. 849–863, 1986.

[27] J. M. Snyder and J. F. Wilson, "Dynamics of the elastica with end mass and follower loading," *ASME J. App. Mech.*, vol. 57, no. 1, pp. 203–208, 1990.

[28] M. W. Spong and M. Vidyasagar, *Robot Dynamics and Control*. New York: Wiley, 1989.

[29] I. D. Walker and M. W. Hannan, "A novel elephant's trunk robot," in *Proc. IEEE/ASME Intl. Conf. on Advanced Intelligent Mechatronics (AIM)*, Atlanta, GA, Sept. 1999, pp. 410–415.

[30] J. F. Wilson, U. Mahajan, and S. A. Wainwright, "A continuum model of elephant trunks," *ASME J. Biomech. Eng.*, vol. 113, no. 1, pp. 79–84, 1991.

[31] J. F. Wilson and J. M. Snyder, "The elastica with end-load flip-over," *ASME J. App. Mech.*, vol. 55, no. 4, pp. 845–848, 1988.

Ian A. Gravagne (S'96–M'02) received the B.S. degree in electrical engineering from Rice University, Houston, TX, in 1997 and the M.S. and Ph.D. degrees from Clemson University, Clemson, SC, in 1999 and 2002, respectively.

He is currently an Assistant Professor with the Engineering Department at Baylor University, Waco, TX. His research interests include robot kinematics and dynamics, especially as applied to continuum robots; modeling, analysis, and control of distributed parameter systems; and real-time operating systems.

Christopher D. Rahn received the B.S. degree in mechanical engineering from the University of Michigan, Ann Arbor, in 1985, and the M.S. and Ph.D. degrees in mechanical engineering from the University of California at Berkeley in 1986, and 1992, respectively.

From 1986 to 1989, he worked for as a Research and Development Engineer at Space Systems/LORAL, Palo Alto, CA, working in the area of spacecraft attitude dynamics and control. He was a Faculty Member of the Department of Mechanical Engineering, Clemson University, Clemson, SC, from 1992 to 2000. In 2000, he joined The Pennsylvania State University, University Park, where he is currently a Professor of Mechanical Engineering. His research interests include the dynamic modeling, analysis, and control of distributed nonlinear systems with application to robotics, mechatronics, and manufacturing.

Ian D. Walker (S'84–M'89–SM'02) received the B.Sc. degree in mathematics from the University of Hull, U.K., in 1983, and the M.S. and Ph.D. degrees in electrical engineering, from the University of Texas at Austin, in 1985, and 1989, respectively.

From 1989 to 1997, he was with the Department of Electrical and Computer Engineering, Rice University, Houston, TX, where he held positions of Assistant and Associate Professor. Since 1997, he has been with the Department of Electrical and Computer Engineering, Clemson University, Clemson, SC, where he currently holds the position of Professor. His research interests are in the areas of robotics, particularly kinematically redundant robots; robot reliability and fault detection; and biologically inspired robots.

Dr. Walker is a member of Sigma Xi, Beta Alpha Phi, Eta Kappa Nu, Phi Kappa Phi, and Tau Beta Pi.